Tectonophysics 694 (2017) 319–331

Contents lists available at ScienceDirect

Tectonophysics

journal homepage: www.elsevier.com/locate/tecto

Mantle-derived helium in foreland basins in Xinjiang, Northwest China

Sheng Xu [a,b], Guodong Zheng [a,*], Jianjing Zheng [a], Shixin Zhou [a], Pilong Shi [c]

[a] Key Laboratory of Petroleum Resources, Gansu Province/Key Laboratory of Petroleum Resources Research, Institute of Geology and Geophysics, Chinese Academy of Sciences, Lanzhou 730000, China
[b] Scottish Universities Environmental Research Centre, East Kilbride G75 0QF, UK
[c] Center for Earth Observation and Digital Earth, Chinese Academy of Sciences, Beijing 100094, China

ARTICLE INFO

Article history:
Received 27 January 2015
Received in revised form 2 November 2016
Accepted 13 November 2016
Available online 15 November 2016

Keywords:
Natural gas
Mantle He
Compression tectonics
Foreland basin
NW China

ABSTRACT

Hydrocarbon-rich natural gases from the Tarim, Junggar, Turpan-Hami and Santanghu basins in Xinjiang, Northwest China have measured $^3He/^4He$ ratios from 0.01 to 0.6 times higher than the atmospheric value, indicating 0–7% helium derived from the mantle. The mantle-derived helium is high in foreland basins associated with the Tianshan, Kunlun and Zhayier-Halalate orogenic mountains, but low towards the center of basins. This spatial distribution suggests that the mantle-derived helium originates either from fluids or small scale melts in the upper asthenospheric or lithospheric mantle which have found pathways into the root zones of the major faults defining these mountains, but do not significantly move into the basins themselves. During upward transport to near the surface, the mantle-derived helium is significantly diluted by radiogenic helium produced in the crust. Despite the lack of recent magmatic activity or extensional tectonics within the basins, this pattern shows strong evidence that the major faults play an important role in mantle-derived components degassing from the mantle to the surface.

© 2016 Elsevier B.V. All rights reserved.

1. Introduction

The terrestrial $^3He/^4He$ ratio (R) varies from a typical radiogenic value of 0.01–0.05 R_a (where R_a is the atmospheric $^3He/^4He$ ratio of 1.4×10^{-6}), produced through the decay of radioactive elements uranium and thorium in the crust, to ~8 R_a in the mantle (e.g., Mamyrin and Tolstikhin, 1984). Therefore, R is a powerful indicator to quantitatively and qualitatively discern changes in the balance between the crustal and mantle-derived volatiles that contribute to the total volatile inventory. It is well documented that the mantle-derived helium has a close relationship with Cenozoic magmatic/volcanic activity and can occur in areas of extensional tectonic activity (Sano et al., 1984; O'Nions and Oxburgh, 1988; Kennedy and van Soest, 2006). On the other hand, since Kennedy et al. (1997) first reported high $^3He/^4He$ ratios along the San Andreas Fault, mantle-derived helium has been observed in areas of tectonic compression or non-volcanic activity (Doğan et al., 2006, 2009; Umeda et al., 2008; Umeda and Ninomiya, 2009; Umeda et al., 2013; Burnard et al., 2012; Klemperer et al., 2013). In these areas, it was found that the mantle-derived helium is transported from the mantle through deep fault fractures.

For gases sampled from surface springs and fumaroles, correction of measured $^3He/^4He$ values for possible atmospheric contamination (R_c) is essential. All the data presented here are sampled at the well-head of oil/gas wells, so that air-contamination is far less likely. Nonetheless, as a unique proxy for the mantle-derived component, $^3He/^4He$ ratios of natural gases have been extensively investigated in China during the last 30 years (i.e., Xu, 1994; Xu et al., 1995, 1998; Du et al., 1998; Zheng et al., 2004, 2005; Tao et al., 2005). In sedimentary basins along the eastern Chinese coast, the R_c/R_a and R/R_a values are generally high (>1) due to the wide occurrence of Cenozoic magmatic activity and extensional tectonics. On the other hand, the R_c/R_a and R/R_a values in sedimentary basins in central China (i.e., the Sichuan and Ordos basins) are typical of a crustal-radiogenic helium component. In the sedimentary basins of northwestern China, the R_c and R values lie between those found in central and eastern China. Although the majority of natural gases in northwestern China have R_c/R_a and R/R_a values (<0.1) close to typical crustal radiogenic helium, a few samples have elevated R/R_a values up to 0.3, which were attributed to the presence of a mantle-derived component (Xu, 1994; Xu et al., 1995, 1998; Du et al., 1998). With the development of oil/natural gas exploration during the last decade, more commercial oil/gas wells have entered production and extensive sampling has become available. As a result, additional elevated $^3He/^4He$ ratios have been observed (Zheng et al., 2004, 2005; Tao et al., 2005; Zhang et al., 2005a), confirming the contribution of mantle-derived helium in the sedimentary basins. However, it has not been documented how the mantle-derived helium occurs in such thickened crust which, in non-volcanic areas, is a result of tectonic compression and associated with large orogenic belts surrounding the sedimentary basins. Thus, based on datasets newly analyzed and previously

* Corresponding author.
E-mail address: gdzhbj@mail.iggcas.ac.cn (G. Zheng).

http://dx.doi.org/10.1016/j.tecto.2016.11.015
0040-1951/© 2016 Elsevier B.V. All rights reserved.

published, this paper examines the regional spatial distribution of $^3He/^4He$ ratios in the Tarim, Junggar, Turpan-Hami and Santanghu sedimentary basins of Xinjiang to understand the relationships between $^3He/^4He$ ratios and tectonic activity in the orogenic belts.

2. Geological backgrounds

Xinjiang is the largest province (1.665 million km^2) in China. It has five major sedimentary basins (Fig. 1): Tarim (560,000 km^2), Junggar (134,000 km^2), Turpan-Hami (53,500 km^2), Yili (38,600 km^2) and Santanghu (23,000 km^2) (e.g., Guo et al., 2006; Qiu et al., 2008; Xu et al., 2001; Zhao et al., 2003; Fu et al., 2003; Zhu et al., 2009; Yu et al., 2012; Tao et al., 2013; Gao et al., 2013; Jiang et al., 2013). The tectonic summary is as follows: Since the Hercynian, western China was located on the southern margin of the Eurasian plate, controlled by the multi-stage subduction of Tethys. With the extinction of the ancient Asian Ocean in the Late Carboniferous–Early Permian periods and the closure of eastern parts of Paleo-Tethys in the Late Triassic epoch, small cratons such as Tarim, North China, and Yangtze collided. This resulted in a series of geological and tectonic activities including the uplift of Hercynian–Indo orogenic belts, the formation of foreland basins, and thrust faults along the peripheral Tarim basin. During the Himalayan period extinction of Neo-Tethys subduction, the India–Tibet collision, and internal deformation within the Eurasia continent occurred. Due to uplift of the Tibetan plateau, the ancient Tianshan, Qilian and Kunlun orogenic belts were reactivated, and the Tarim and Junggar basins underwent rapid subsidence. This resulted in the formation of foreland basins in a ring peripheral to the Tibetan Plateau. The reactivated Himalayan foreland basins and thrust faults were developed on previously formed forelands, creating a terrestrial sedimentary system, and thrust–strike slip faults (Gao et al., 2013; Jiang et al., 2013).

The Tarim basin is bounded by the Tianshan Mountains to the northwest and north, and by the Kunlun and Altun mountains to the south (Fig. 2A). The strata consist of Precambrian–Permian marine and Mesozoic–Cenozoic terrestrial sedimentary rocks up to 10,000 m thick. The foreland sub-basins are distributed in front of the Tianshan and Kunlun Mountains. The Junggar basin, bounded by the Qinggelidi Mountains to the northeast, by the Yilinheibiergen and Bogda Mountains of the Tianshan range to the south, and by the Zhayier-Halalate Mountains to the northwest (Fig. 2B) is an upper Paleozoic, Mesozoic and Cenozoic superimposed basin with stratigraphy ranging from the Carboniferous to the Cretaceous (Cao et al., 2012). The foreland sub-basins are distributed in front of the Tianshan and Zhayier-Halalate Mountains. The Turpan-Hami and Santanghu basins are typical foreland basins located on the southern and northern side of the eastern Tianshan (Bogda) Mountains, respectively. The Turpan-Hami basin is bounded by the Tianhsan (Bogda) Mountains to the north and by the Jueluotage Mountains to the south (Fig. 2C). The Santanghu basin is bounded by the Suhaitu Mountains to the northeast and by the Moqin-Urals to the southwest (Fig. 2D). Each basin can be divided into several sub-structural units (Tao, 2010; Zhang et al., 2010; Cao et al., 2012; Li et al., 2013).

The last extensive igneous activities in Xinjiang are the Late Devonian to Late Carboniferous (361–306 Ma) volcanic rocks, mainly consisting of basalt, trachyte, trachy-andesite, andesite and rhyolite (Zhu et al., 2009; Zhang et al., 2010; Yu et al., 2012). In addition, as shown in Fig. 1, Tertiary-Quaternary volcanics scattered in transition zones between Tianshan Mountains and Tarim basin (20–40 Ma in TY and PQ), between Kunlun Mountains and Tarim basin (20–0.1 Ma in KXW, DHLT, PL and ASKL), and between Altai Mountains and Junggar basin (17 Ma in HLQL) (Turner et al., 1996; Liu and Maimaiti, 1989; Luo et al., 2003; Chung et al., 2005; Huang et al., 2006). Most earthquakes in the study area occur within the orogenic

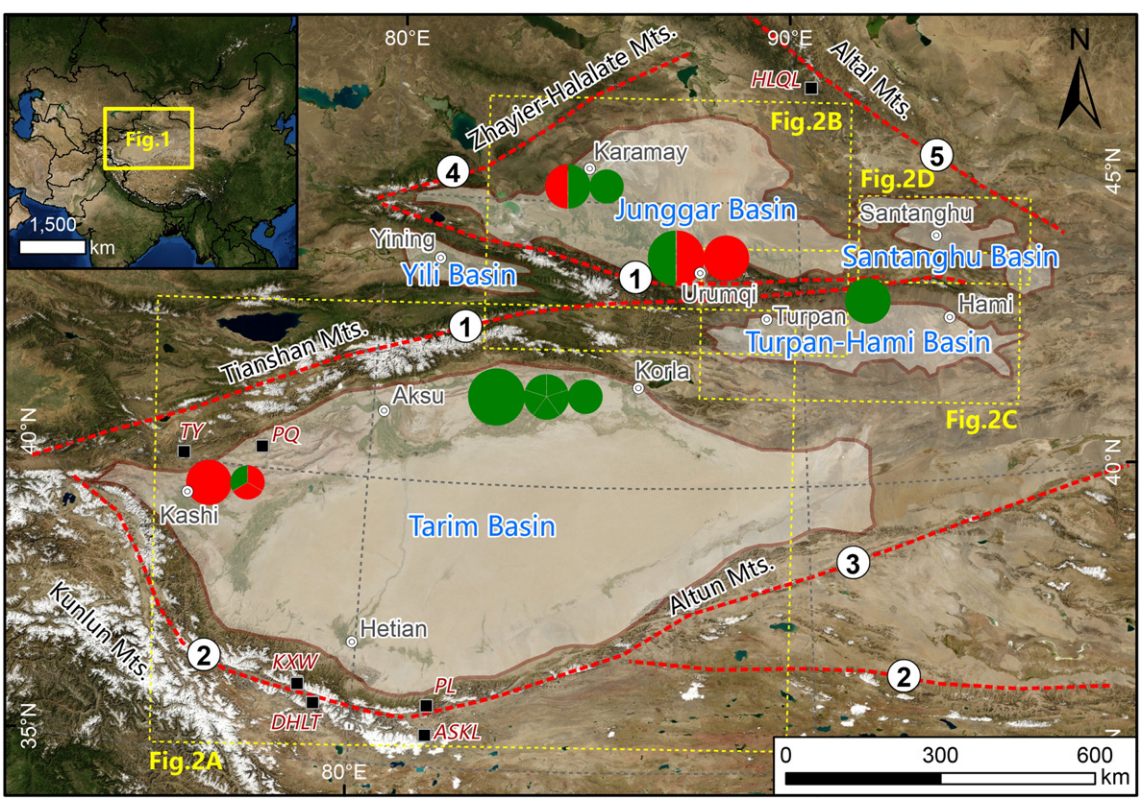

Fig. 1. Simplified map of northwestern China showing major sedimentary basins and adjacent orogenic mountains. The circles indicate the orogenic belts: 1, Tianshan; 2, Kunlun; 3, Altun, 4, Zhayier-Halalate; and 5, Altai Mountains. The squares denote occurrence of the Cenozoic volcanic rocks; PG: Piqiang, TY: Tuoyun, KXW: Kangxiwa, PL: Pulu, DHLT: Dahongliutan, ASKL: Ashikule, HLQL: Halaqiaola. Occurrence of mantle-derived helium is shown with red or green Pie chart (counted numbers, see legend in Fig. 2 for details).

belts and in the transition zones between the mountain and the adjacent basin, especially concentrated in the Tianshan, Pamir, and Kunlun mountains and rarely distributed in the basins (e.g., Fu et al., 2003; Xu et al., 2001). Geophysical evidence shows that the crustal thickness under the orogenic belts today is approximately > ~ 50 km, somewhat greater than the adjacent basins (40–50 km) (Gao et al., 2013; Jiang et al., 2013). The crust in Xinjiang is ~10–20 km thicker than in eastern and central China.

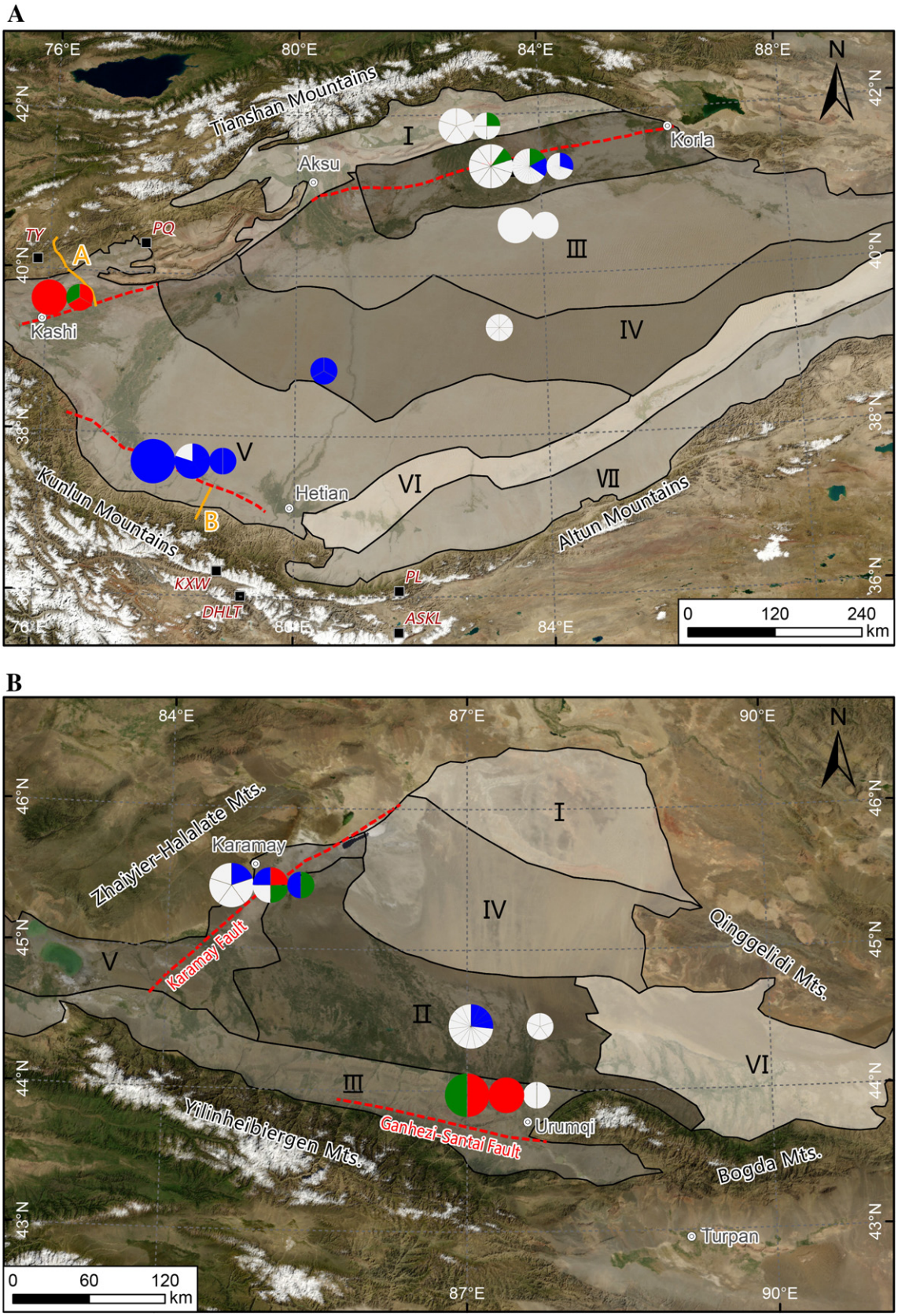

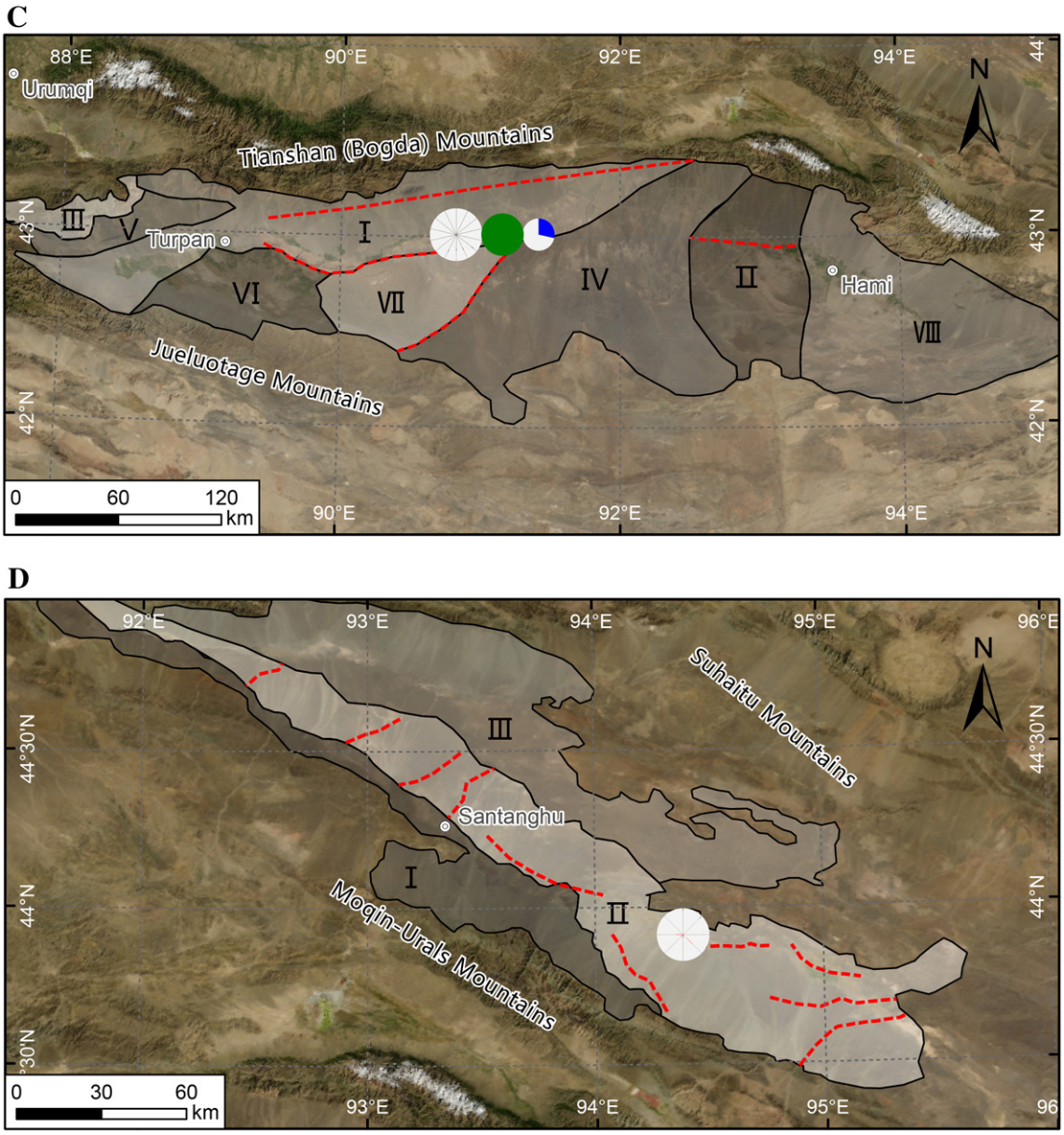

Fig. 2. $^3He/^4He$ distribution in natural gases from sedimentary basins in Xinjiang. Maps are modified from Cao et al. (2012), Li et al. (2013), Tao (2010) and Zhang et al. (2010). The dotted red lines denote the thrust faults and other type of faults. (A) Tarim basin: I. Kuqa depression; II. Tabei uplift; III. North depression; IV. Tazhong uplift; V. Southwest depression; VI. Tanan uplift; VII. Southeast depression. Two seismic profiles are shown in A and B (Gao et al., 2013; Jiang et al., 2013). (B) Junggar basin: I. Wulungu depression; II. Central depression; III. Southern depression; IV. Luliang super uplift; V. West super uplift; VI. East super uplift. (C) Turpan-Hami basin: I. Turpan depression; II. Hami depression; III. Keyayi depression; IV. Liaodun uplift; V. Buerjia uplift; VI. Luxi uplift; VII. Takequan uplift; VIII. Huangtian uplift. (D) Santanghu basin: I. Southwest thrust fault zones; II. Central depression; III. Northeast thrust fault zones. The large, medium, and small Pie charts denote air-corrected $^3He/^4He$ (R_c/R_a), non-air-corrected $^3He/^4He$ but $^{40}Ar/^{36}Ar > 500$ (R/R_a), and non-air-corrected $^3He/^4He$ but $^{40}Ar/^{36}Ar < 500$ or no $^{40}Ar/^{36}Ar$ (R/R_a), respectively. The exploded Pie with different colors shows the numbers of sample with different R_c/R_a or R/R_a (>0.3 in red, 0.3–0.1 in green, 0.1–0.05 in blue and <0.05 in white). Note that the sample locations in each sub-tectonic unit are under the Pie charts, and that we do not have authorization to provide a more accurate location.

3. Sampling and experiments

All natural gas samples were collected into a 1 l volume stainless steel container with valves in both sides connected directly to the well-head. After being flushed with gas for several minutes, the gas sample was collected. Although during sampling of high pressure wells air contamination at the sampling point is unlikely, it is by no means impossible for entrainment of atmosphere or water derived gases to occur if the well casing is compromised anywhere in the subsurface. To assess any possible air contamination $^4He/^{20}Ne$ or, if not available, $^{40}Ar/^{36}Ar$ ratios and helium concentration are used as a proxy (e.g., Sano et al., 1987).

About ~1 cm^3 STP natural gas was introduced into a vacuum system to separate helium, neon and argon from other noble gases (krypton and xenon) and active gases (carbon dioxide, hydrocarbons, nitrogen, etc.). $^3He/^4He$, $^4He/^{20}Ne$ and $^{40}Ar/^{36}Ar$ ratios were determined using a static mass spectrometer (VG5400, Micromass). Air was used as a standard for $^3He/^4He$, $^4He/^{20}Ne$ and $^{40}Ar/^{36}Ar$ analyses. Repeat measurements of air standard showed ~10% uncertainty for $^4He/^{20}Ne$ and 3% for $^{40}Ar/^{36}Ar$ ratios. In addition, typical errors of gas chromatographic analysis on major gas (hydrocarbons) and trace gas (N_2, CO_2, He) compositions were approximately 5% and 10%, respectively. Detailed description of the experimental procedure can be found elsewhere (Xu, 1994).

Table 1
$^3He/^4He$ ratios in sedimentary basins from Xinjiang, Northwest China.

No.	Well name	Reservoir[a]	Depth (m)	CO_2 (%)	HC[b] (%)	N_2 (%)	He (ppm)	$\delta^{13}C_{CH4}$ (‰)	$\delta^{13}C_{CO2}$ (‰)	$(^3He/^4He)_{measured}/(^3He/^4He)_{air}$ (R/R_a)	$^4He/^{20}Ne$	$^{40}Ar/^{36}Ar$	Air-corrected $(^3He/^4He)_{measured}/(^3He/^4He)_{air}$[c] ($R_c/R_a$)	Mantle He[d] (%)	Reference[e]
Tarim basin (37°–42°N, 76°–90°E)															
Kuqa depression															
1	KL2	N	3888–3895	0.94	98.85	0.60		−27.3		0.029					(3)
2	DW102	N		0.04						0.108					(3)
3	Dabei2	K	5658–5670					−30.8		0.038		1068		0	(4)
4	Dabei2	K	5658–5670							0.038 ± 0.002					(6)
5	Dawan105-25	N-K	367–396		89.29		72	−28.5		0.041		1120		0	(4)
6	Dina2	N	4597–4875							0.018		536		0	(5)
7	Dina2	N	4598–4876							0.018 ± 0.001					(6)
8	DN22	E	4748–4774							0.020		647		0	(5)
9	DN201	E	4980–4990							0.018		645		0	(5)
Tabei uplift															
10	S79CH	O	5705–6185							0.031 ± 0.003	620	365	0.031 ± 0.004	0	(1)
11	TK923H	T	4733–5010							0.041 ± 0.003	180	410	0.039 ± 0.005	0	(1)
12	S48	O	5364–5370							0.025 ± 0.003	2540	484	0.025 ± 0.004	0	(1)
13	TK471X	O	5507–5595							0.030 ± 0.003	900	476	0.030 ± 0.004	0	(1)
14	TP37	O	6804–6940							0.049 ± 0.003	530	661	0.048 ± 0.006	0	(1)
15	TK864	O	5521–5540							0.045 ± 0.003		433			(1)
16	TK718	O	5716–5732							0.018 ± 0.003		387			(1)
17	TK635H	O	5557–5565							0.031 ± 0.003		385			(1)
18	TK217	O	5491–5510							0.043 ± 0.003		391			(1)
19	TK763CH	O	5504–5559							0.038 ± 0.003		408			(1)
20	TK730	O	5519–5561							0.050 ± 0.003		365			(1)
21	YK12	K	5253–5264							0.250 ± 0.003		3711		3	(1)
22	YK6H	K	5292–5293							0.261 ± 0.003		2896		3	(1)
23	YK19	K	5331–5334							0.204 ± 0.003		3893		2	(1)
24	DH1	C		6.67	92.37		2300	−41.3		0.047		549		0	(2)
25	DH4	C		25.34	40.94		3964	−44.5		0.016		482			(2)
26	JF100	T	4430	0.36	99.60	2.70	853	−35.9		0.044		766		0	(2)
27	JF123	O		0.45	99.35		1808	−35.1		0.029		945		0	(2)
28	JF131	T	4251	1.06	99.90		659	−36.4		0.045		595		0	(2)
29	YM7	E	4700	0.31	97.92		634	−34.7		0.044		513		0	(2)
30	YM2	N		0.32	97.74	1.91				0.029					(2)
31	LN14	C	5266	2.18	98.72		1029	−37.1		0.043					(2)
32	LN10	O		2.07	93.47	4.45	2428	−37.3		0.059					(2)
33	LN17	C-O		24.24	75.76		1897	−34.7		0.034		756		0	(2)
34	LN5	J		0.16	99.84		463	−36.4		0.056		1273		0.1	(2)
35	LN26	T		1.64	91.76	6.60	5304	−37.2		0.061		753		0.1	(2)
36	LN55	T		2.05	83.85	4.10	9284	−37.1		0.050					(2)
37	LN2-24-2	T		2.17	97.83		276	−35.5		0.036					(2)
38	LN2-24-2	T		1.50	92.00		240			0.035 ± 0.003	7400		0.035 ± 0.005	0	(7)
39	LN2-2-3	T		2.76	97.23		356	−37.1		0.040					(2)
40	LN204	T			100.00		383	−35.3		0.037		801		0	(2)
41	LN2-2	T		3.57	96.33		8306	−37.1		0.042		689		0	(2)
42	LN3-1	T		1.63	98.34		720	−37.9		0.041					(2)
43	LN33-1	J		0.62	99.84	4.62	220	−39.4		0.076		930		0.3	(2)
44	LN34-2	J		1.59	98.30		515	−39.2		0.066					(2)
45	LN22	T	4638	2.83	99.70		657	−36.4		0.040		503		0	(2)
46	T1		4847	0.38	99.61		61			0.018					(2)
47	ShaC2	O	5392	0.40	99.52	0.01		−41.1		0.150		1735		1	(2)
48	ShAC7	€	5416	3.20	96.52			−42.4		0.157		2334		1	(2)
49	YM7	K	4945–4949							0.057					(3)
50	YM9									0.058					(3)

(continued on next page)

Table 1 (*continued*)

No.	Well name	Reservoir[a]	Depth (m)	CO_2 (%)	HC[b] (%)	N_2 (%)	He (ppm)	$\delta^{13}C_{CH4}$ (‰)	$\delta^{13}C_{CO2}$ (‰)	$(^3He/^4He)_{measured}/(^3He/^4He)_{air}$ (R/R_a)	$^4He/^{20}Ne$	$^{40}Ar/^{36}Ar$	Air-corrected $(^3He/^4He)_{measured}/(^3He/^4He)_{air}$[c] ($R_c/R_a$)	Mantle He[d] (%)	Reference[e]
51	YM6									0.058					(3)
52	YH301-4									0.036					(3)
53	T1									0.029					(3)
54	T1		4837–4847	0.40	97.10		46			0.018 ± 0.003	1500		0.018 ± 0.003	0	(7)
55	S3									0.043					(3)
56	YD2									0.050					(3)
57	Jiefang138	T3	4556–4563				843	−35.1		0.048		343			(4)
58	Yangtake5	E	5310–5315		83.97		314	−33.4		0.048		655		0	(4)
59	Lunnan10-2				77.64		814	−37.1		0.038		624		0	(4)
60	Lunnan3-H5				84.65		949	−35.1		0.060		959		0.1	(4)
61	Lunnan33-1				71.34		220			0.076					(4)
62	Lunnan2-25-H1				90.55		655	−34.1		0.041		862		0	(4)
63	Lungu13							−34.7		0.031		415			(4)
64	Lungu18							−36.9		0.025		481			(4)
65	YH23-1-5	N	4946–4988							0.025		613		0	(5)
66	YH1	E	5451–5466							0.027		727		0	(5)
67	YH3	E	5139–5165							0.023		504		0	(5)
68	YTK-1	K	5329–5333							0.050		765		0	(5)
69	QL1	K	5761–5764							0.038		624		0	(5)
70	YH23-2-10	E + K	5135–5189							0.021		627		0	(5)
71	YH701	E	5160–5168							0.021		604		0	(5)
72	YH2	N	4954–4963							0.023		618		0	(5)
73	Shacan2	O	5300	4.40	88.50		490			0.159 ± 0.005	16,000		0.16 ± 0.02	1	(7)
74	Ln17	O		3.30	97.60		280			0.032 ± 0.002	6800		0.032 ± 0.004	0	(7)
75	Yinmai2			6.40	74.20		680			0.029 ± 0.003	9300		0.029 ± 0.004	0	(7)
76	LN3-H5	T	5183–5383							0.059					(8)
77	LN2-25-H1	T	4944–5260							0.041					(8)
78	JF138	T	4556–4563							0.031					(8)
79	LG18	O	5462–5547							0.025					(8)
80	T814(K)	O	5574–5670							0.021 ± 0.002					(9)
81	T_7-615	O	5521–5637							0.028 ± 0.002					(9)
82	T401	O	5367–5580							0.031 ± 0.002					(9)
83	T913	O	5825							0.031 ± 0.003					(9)
84	TK305	O	5407–5461							0.041 ± 0.002					(9)
85	TK657	O	5685–5775							0.059 ± 0.003					(9)
North depression															
86	HD1-1H	C	5113–5449							0.018		626		0	(5)
87	HD1-1H	C	5113–5449							0.019					(8)
Tazhong uplift															
88	JL107	C	5406	0.38	99.40	2.43	2045	−33.9		0.015		820		0	(2)
89	TZ1	O	3666	0.32	83.55	16.12	540	−43.4		0.033		923		0	(2)
90	TZ1	O	3650							0.033		923		0	(5)
91	TZ4-7-H22	C	3605							0.027		672		0	(5)
92	TZ4-401-H2	C	3724							0.029		662		0	(5)
93	TZ4-17-7	C	3521–3542							0.025		675		0	(5)
94	TZ111	S	4598–4964							0.022		554		0	(5)
95	TZ4	C	4350							0.028		890		0	(5)
96	Ma2	C	1462–1501					−36.2		0.076					(10)
97	Ma4	O	2380–2395	0.20	83.30	13.00		−37.8		0.077					(10)
98	M401	O	2351–2382					−37.6		0.083					(10)
Southwest depression															
99	Ke243	N	3839	0.03	99.92			−37.8		0.056					(2)
100	Ke2	N	3153		99.99			−38.2		0.044		855		0	(2)
101	Ke8	N	3304	0.02	99.98			−37.5		0.056		982		0.1	(2)

102	Ke8	N	3283–3304		96.70		50			0.056 ± 0.004	3100		0.056 ± 0.007	0.1	(7)
103	Ke701	N	3839	3.99	95.43	3.99		−38.1		0.061		683		0.1	(2)
104	Ke18	N	3272	3.98	96.00			−38.5		0.052					(2)
105	Ake1	K	3226–3341							0.593					(4)
106	Ake1	K	3226–3341	11.44	81.50	7.97		−23	−8.6	0.596 ± 0.018		1438		7	(6)
107	Ake1	T		13.33	77.37	8.97	930			0.549					(11)
108	KKY333X4-1							−37.8		0.062		944		0.1	(4)
109	Keshen101	E	6354–6363	0.52		2.38				0.098 ± 0.004		871		0.1	(6)
110	Qu3	C								0.170					(11)
Junggar basin (44°–46°N, 82°–90°E)															
Central depression															
111	Cai156	J		0.23	89.92	5.20	370			0.033 ± 0.003	7354	1042	0.033 ± 0.004	0	(1)
112	Cai27	J		0.22	73.92	13.06	343			0.048 ± 0.003	180	1099	0.046 ± 0.006	0	(1)
113	Cai514	J					1380			0.047 ± 0.003	540	472	0.047 ± 0.006	0	(1)
114	Cai201	J		0.21	74.61	13.52	425			0.076 ± 0.003	261	929	0.075 ± 0.008	0.3	(1)
115	C121	J		0.83	91.58	3.58	86			0.033 ± 0.005	303	311	0.032 ± 0.006	0	(1)
116	Quan6	J		0.05	73.72	20.51	1106			0.014 ± 0.001	999	508	0.014 ± 0.002	0	(1)
117	C3150	J		0.17	93.40	2.91	160			0.052 ± 0.001	1238	1356	0.052 ± 0.005	0.1	(1)
118	Dixi12-Dx2500	J					316			0.023 ± 0.001	252	334	0.022 ± 0.003	0	(1)
119	Cai401	J		0.06	91.83	3.88	166			0.051 ± 0.001	876	648	0.051 ± 0.005	0.1	(1)
120	Cai140	J			12.11	82.70	158			0.060 ± 0.001	12	297	0.036 ± 0.006	0	(1)
121	Cai506	J		0.21	52.33	44.74	81			0.046 ± 0.001	337	310	0.045 ± 0.005	0	(1)
122	Cai508	J		0.02	92.26	3.43	2030			0.028 ± 0.001	244	777	0.027 ± 0.003	0	(1)
123	Di20	J		0.04	93.16	3.05	1074			0.053 ± 0.001	448	353	0.052 ± 0.005	0.1	(1)
124	Cai137	J		0.09	89.01	5.21	280			0.030 ± 0.001	293	765	0.029 ± 0.003	0	(1)
125	Cai510	J		0.01	91.60	3.98	1068			0.019 ± 0.001	682	686	0.019 ± 0.002	0	(1)
126	Mo11	J	4175							0.021 ± 0.001					(1)
127	Pen5	J	4250							0.043 ± 0.001					(1)
128	Dixi14	C	3660							0.024 ± 0.002					(1)
129	Lu124	K	1005							0.043 ± 0.009					(1)
130	DX1001	C	3030							0.024 ± 0.002					(1)
Southern depression															
131	Sha1955	J					2360			0.186 ± 0.051	2113	329	0.186 ± 0.051	2	(1)
132	Bei16	P	2217–2225		96.30		51			0.306 ± 0.005	1800		0.306 ± 0.005	3	(13)
133	Bei16	P	2217–2225							0.302		592		3	(12)
134	B2032			0.04	87.25	4.93	137			0.190					(13)
135	Du85	N	575–597							0.034					(14)
West super uplift															
136	Huo11	P	1549–1629		96.40		22			0.048 ± 0.003	450		0.047 ± 0.006	0	(7)
137	Che30	C	2363–2375	0.73	97.00		120			0.037 ± 0.003	6300		0.037 ± 0.005	0	(7)
138	Che30	C	2363–2375							0.047		979			(12)
139	807	P	2317–2347		93.50		220			0.076 ± 0.003	15,000		0.076 ± 0.008	0.3	(7)
140	807	P	2317–2347							0.089		1674			(12)
141	307				94.00		16			0.032 ± 0.003	900		0.032 ± 0.004	0	(7)
142	87				96.80		33			0.024 ± 0.003	2100		0.024 ± 0.004	0	(7)
143	Che32	C	3345–3352							0.093		476			(12)
144	Hong60	C	2274–2575							0.386		1125		4	(12)
145	Xia40	P	4831–4886							0.133		725		1	(12)
146	5135			6.13	87.33					0.220					(13)
Turpan-Hami basin (42°–43°N, 88°–94°E)															
Turpan depression															
147	Pubeil6	J	3547.8							0.036 ± 0.001	249	458	0.035 ± 0.004	0	(1)
148	Le101	J	2707–2808							0.013 ± 0.001	567	625	0.012 ± 0.002	0	(1)
149	Qiudong7	J	3107–3198							0.028 ± 0.001	925	595	0.028 ± 0.003	0	(1)
150	Pu10–6	J								0.095 ± 0.008	6	296	0.046 ± 0.006	0	(1)
151	Yan6-20	E	1577–1624							0.037 ± 0.002	155	316	0.035 ± 0.004	0	(1)

(continued on next page)

Table 1 (*continued*)

No.	Well name	Reservoir[a]	Depth (m)	CO_2 (%)	HC[b] (%)	N_2 (%)	He (ppm)	$\delta^{13}C_{CH4}$ (‰)	$\delta^{13}C_{CO2}$ (‰)	$(^3He/^4He)_{measured}/(^3He/^4He)_{air}$ (R/R_a)	$^4He/^{20}Ne$	$^{40}Ar/^{36}Ar$	Air-corrected $(^3He/^4He)_{measured}/(^3He/^4He)_{air}$[c] ($R_c/R_a$)	Mantle He[d] (%)	Reference[e]
152	Yan17	K	1770–1797							0.069 ± 0.001	6	308	0.016 ± 0.002	0	(1)
153	Wen8-35	J	2350–2410							0.019 ± 0.001	554	506	0.018 ± 0.002	0	(1)
154	Wen311	J	2626–2714							0.088 ± 0.003	5	298	0.035 ± 0.004	0	(1)
155	Ke7	J	1841–1848		94.60		110			0.028 ± 0.004	6100		0.028 ± 0.005	0	(7)
156	Ke7	J	1841–1848							0.050					(12)
157	Taican1	J	2808–3247		92.40		160			0.018 ± 0.001	3600		0.018 ± 0.002	0	(7)
158	Wenxi7-1	J			17.20		510			0.034 ± 0.003	3000		0.034 ± 0.004	0	(7)
159	Wen21	J			92.00		550			0.032 ± 0.002	7600		0.032 ± 0.004	0	(7)
160	Lin36	J	2890–2951		96.50		170			0.022 ± 0.001	3900		0.022 ± 0.002	0	(7)
161	Shengnan1	J	2320–2330		94.40		33			0.039 ± 0.002	1300		0.039 ± 0.004	0	(7)
162	QD3	J	3332–3409							0.025					(12)
163	QD3	J	3105–3141							0.055					(12)
164	L3	J	2411–2416							0.033					(12)
165	S6-17	J	2952–3062							0.061					(12)
166	S13-15	J	3086–3100							0.031					(12)
167	L25	J	2737–2747							0.038					(12)
168	Hongtai2	J		0.11	85.47	3.36	693			0.120		571		1	(13)
Santanghu basin (43°–45°N, 92°–96°E)															
Central depression															
169	Ma17	P	1515–1543							0.109 ± 0.006	4	297	0.043 ± 0.005	0	(1)
170	Ma18	P	1423–1445							0.045 ± 0.004	419	504	0.044 ± 0.006	0	(1)
171	Ma19	P	1535–1558							0.051 ± 0.003	28	310	0.041 ± 0.005	0	(1)
172	Niu16-8	J	998–1025							0.029 ± 0.001	1387	363	0.029 ± 0.003	0	(1)
173	Tangcan1	J	2089–2092							0.021 ± 0.001	678	491	0.021 ± 0.002	0	(1)
174	Niu103	J								0.037 ± 0.002	184		0.035 ± 0.004	0	(1)
175	BA27									0.022 ± 0.001	732	414	0.022 ± 0.002	0	(1)
176	Niu111	J	1000–1012							0.036 ± 0.001	20	302	0.021 ± 0.002	0	(1)

[a] Abbreviation of reservoir strata. €, Cambrian; C, Carboniferous; E, Eocene; J, Jurassic; K, Cretaceous; N, Neogene; O, Ordovician; P, Permian; S, Silurian and T, Triassic.

[b] Sum of light hydrocarbon components (methane, ethane, propane, n-butane and i-butane).

[c] Air-corrected $(^3He/^4He)_{measured}/(^3He/^4He)_{air} = [(^3He/^4He)_{measured}/(^3He/^4He)_{air} - r]/[1 - r]$ where $r = (^4He/^{20}Ne)_{air}/(^4He/^{20}Ne)_{measured}$ (Sano et al., 1987).

[d] %mantle He $= [(^3He/^4He)_{corrected} - (^3He/^4He)_{crust}]/[(^3He/^4He)_{mantle} - (^3He/^4He)_{crust}]$ where $(^3He/^4He)_{mantle} = 8\ R_a$ and $(^3He/^4He)_{crust} = 0.05\ R_a$. In case of samples without available $^4He/^{20}Ne$ but $^{40}Ar/^{36}Ar > 500$, the measured $^3He/^4He$ are used for calculation (see text).

[e] (1) This study; (2) Xu et al. (1998); (3) Qin (1999); (4) Zheng et al. (2005); (5) Zhang et al. (2005a); (6) Zhang et al. (2005b); (7) Xu et al. (1995); (8) Zheng et al. (2004); (9) Duan et al. (2007); (10) Wang et al. (2008); (11) Liu et al. (2009); (12) Xu (1994); (13) Tao et al. (2005); (14) Dai et al. (2012).

4. Results

The R/R_a and some $^4He/^{20}Ne$ and $^{40}Ar/^{36}Ar$ ratios, together with previously published data, are summarized in Table 1. Our new R/R_a and $^{40}Ar/^{36}Ar$ data from 51 gas samples are in good agreement with the previously published datasets. The observed R/R_a, $^4He/^{20}Ne$ and $^{40}Ar/^{36}Ar$ ratios show wide variability from 0.01 to 0.6, from 4 to 16,000 and from 296 to 3893, respectively. The R/R_a ratios are mainly <0.1 in all basins, which are consistent with those observed in the Ordos and Sichuan basins in central China (Xu et al., 1995; Du et al., 1998; Zheng et al., 2005). In contrast, the highest R/R_a ratio (0.6) observed in Tarim basin (sample Nos. 105–107) is obviously higher than those observed in central China, but significantly lower than those observed in natural gases produced in eastern China (Xu et al., 1995; Du et al., 1998; Zheng et al., 2004). In comparison with other areas in China, the relatively lower R/R_a ratios in Xinjiang imply different helium sources and/or tectonics from central and eastern China.

Stratigraphy of the natural gas reservoir in the studied areas varies with different depth and geological periods in each basin. Overall, the observed R/R_a ratio is not clearly correlated with the depth and age of the gas reservoirs. The natural gases in Xinjiang are mainly hydrocarbon-rich with traces of non-hydrocarbon components including CO_2 and N_2. The CO_2 concentrations are usually below 5% with the exception of >10% in a few samples from the Akmomu gas field (sample Nos. 106 and 107), located in the southwestern margin of the Tarim basin, and the Luntai-Donghetang gas field (sample Nos. 25 and 33) in the northern Tarim basin (Xu, 1994; Zhang et al., 2005a; Li et al., 2013).

5. Discussion

5.1. Helium origins in sedimentary basins

In nature, terrestrial helium has three major origins: atmospheric, crustal radiogenic and mantle-derived, each of which has distinct $^3He/^4He$ and $^4He/^{20}Ne$ ratios. The $^4He/^{20}Ne$ ratio is usually considered a proxy of the atmospheric component because neon is mainly atmospheric in origin. In comparison with the $^4He/^{20}Ne$ ratios in atmosphere (0.29) and air-saturated-water (0.32), the $^4He/^{20}Ne$ ratios in natural gases vary from 4 to 16,000, being 10-to-20,000 times higher, indicating <10% to <0.005% air contamination. Similarly high $^4He/^{20}Ne$ ratios have been observed in natural gases in eastern and central China (Xu et al., 1995). Fig. 3 shows the relationship between $^3He/^4He$ and $^4He/^{20}Ne$ ratios. Seven samples (Nos. 120, 150, 152, 154, 169, 171 and 176) that have relatively low $^4He/^{20}Ne$ (4–28), but are still one order of magnitude higher than the atmospheric value, are plotted along the mixing line between air and the crustal component. The low $^{40}Ar/^{36}Ar$ ratios (296–310, which are close to the atmospheric value of 295.5) in these samples support the contribution of the atmospheric noble gas component (Fig. 4), so we do not discuss these samples further. For most samples there is essentially no difference when we correct the observed $^3He/^4He$ ratio for air contamination using available $^4He/^{20}Ne$ ratios (Table 1). For those samples without measured $^4He/^{20}Ne$ ratios, the $^{40}Ar/^{36}Ar$ ratio together with helium concentration can be used to qualitatively assess the atmospheric contribution. Fig. 5 shows a histogram of R_c/R_a and R/R_a in Xinjiang. In the latter case without available $^4He/^{20}Ne$ values, two groups are further divided based on $^{40}Ar/^{36}Ar$ ratios. Most natural gases from Xinjiang have R_c/R_a and R/R_a values <0.05, which can be attributed to a purely crustal-radiogenic origin. However, a number of elevated R_c/R_a (>0.1) observed in the Tarim and Junggar basins (Nos. 73, 131, 132), and some R/R_a values (>0.1) in the Tarim, Junggar and Turpan-Hami basins, indicate an anomalous excess of ^3He which suggests other sources of helium in addition to the crustal-radiogenic component.

In nature, several processes may cause the anomalous excess of ^3He: (1) tritiogenic ^3He produced by the decay of natural and anthropogenic tritium (^3H) in groundwater through reaction $^3H(\beta^-)^3He$; (2) radiogenic

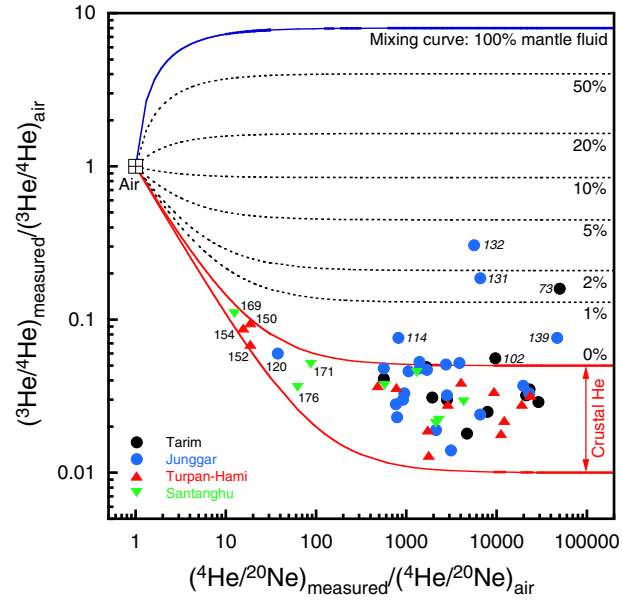

Fig. 3. Relationship between the measured $^3He/^4He$ (R/R_a) and $^4He/^{20}Ne$ ratios in natural gases from the sedimentary basins in Xinjiang.

^3He by the nuclear reaction $^6Li(n,\alpha)^3H(\beta^-)^3He$ in lithium-rich surrounding rocks; (3) ^3He released from pre-eruptive/intrusive mantle-derived rocks in the crust; and (4) ^3He degassing from the mantle. Because we only studied well-gas samples, they are most unlikely to include tritiogenic ^3He from nuclear weapon tests. Below we discuss these other three possible sources for such high $^3He/^4He$ ratios observed in the studied sedimentary basins.

5.1.1. Radiogenic ^3He from lithium-rich surrounding rocks

The radiogenic ^3He can be formed by lithium reacting with neutron through reaction $^6Li(n,\alpha)^3H(\beta^-)^3He$. Thus, the $^3He/^4He$ ratio of radiogenic helium in a rock depends mainly on the concentration of lithium and neutron flux. One of the neutron sources is from cosmic rays. However, such process requires exposure to cosmic rays at subsurface, resulting in no problem for deep gas fields. Instead the major neutron

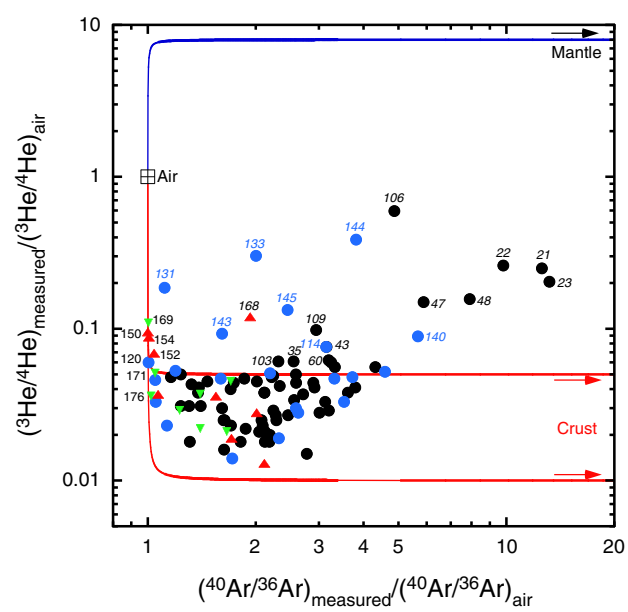

Fig. 4. Relationship between the measured $^3He/^4He$ (R/R_a) and $^{40}Ar/^{36}Ar$ ratios in natural gases from the sedimentary basins in Xinjiang. The symbols are the same as Fig. 3.

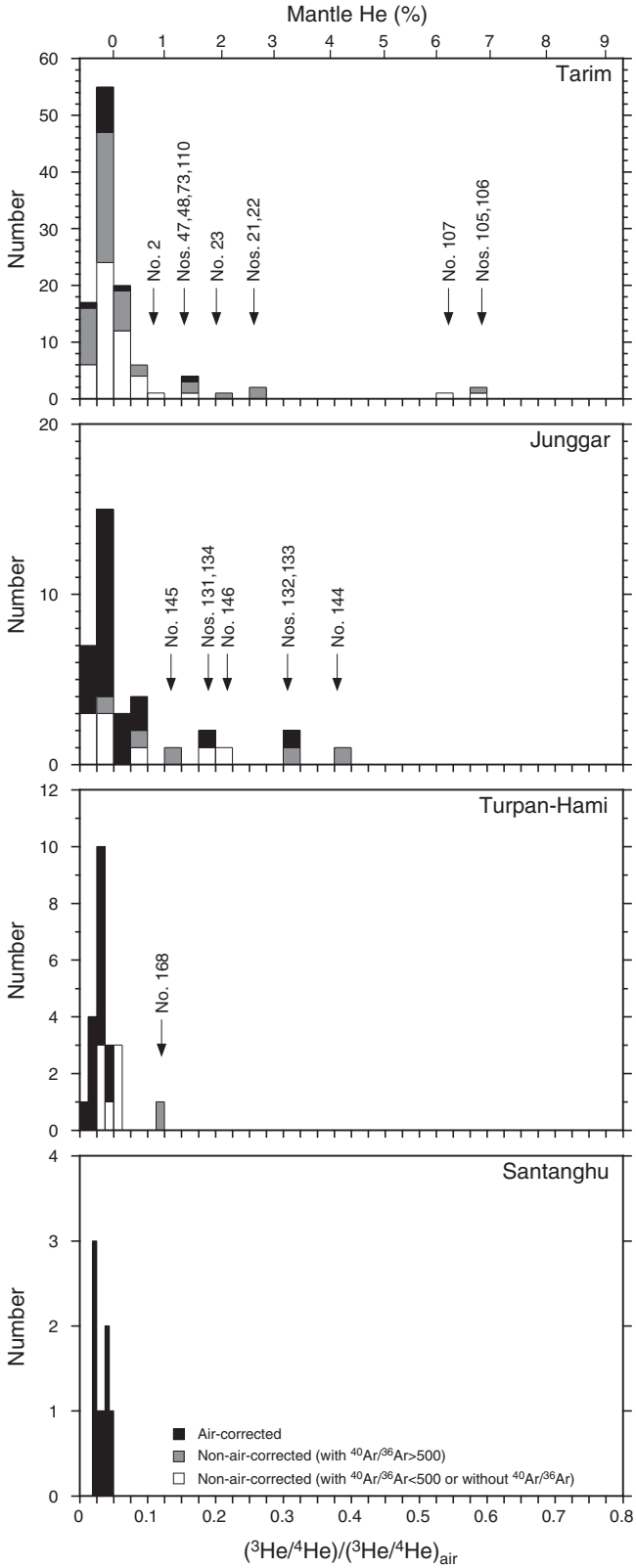

Fig. 5. Histogram of $^3He/^4He$ ratios in natural gases from sedimentary basins in Xinjiang. This includes R_c/R_a (air-corrected $^3He/^4He$), and R/R_a (non-air-corrected $^3He/^4He$ with $^{40}Ar/^{36}Ar > 500$, and that with $^{40}Ar/^{36}Ar < 500$ or without $^{40}Ar/^{36}Ar$).

sources in rock are provided by the radioactive decay of uranium and thorium. Therefore, the $^3He/^4He$ ratio of radiogenic helium in a rock depends mainly on the concentration of lithium, uranium and thorium of the surrounding rocks.

The average crustal concentration of lithium, uranium and thorium results in $^3He/^4He$ range of 0.01–0.05 R_a. However, the $^3He/^4He$ ratio of lithium-rich minerals such as beryl, cordierite, chromite and spodumene has been reported to be up to 7 R_a (Mamyrin and Tolstikhin, 1984, and references therein). Although the lithium concentrations of the basement rock in the studied areas are not available, the lithium content of various igneous and sedimentary rocks in China compiled by several researchers is normally <100 ppm (Li, 1995; Gao et al., 1998). Local uranium and thorium contents from the Junggar basin are found to be consistent with those in sedimentary rocks from five Chinese sedimentary basins (Shen et al., 1983; Tao et al., 2013). As these datasets show the concentrations of uranium, thorium and lithium in Xinjiang and other sedimentary basins are within the ordinary range of crustal chemical compositions, the theoretical calculation (Mamyrin and Tolstikhin, 1984) would result in the $^3He/^4He$ ratio being the same as the typical crustal value. Even in the case of the basement rocks with anomalous lithium content ~100 ppm, the local $^3He/^4He$ ratio of radiogenic helium cannot exceed 0.1 R_a. Thus, it is considered that anomalous ^6Li decay is highly unlikely to be the source of excess ^3He in the natural gas reservoirs.

5.1.2. ^3He from older igneous rocks

The most extensive and latest igneous activities within the studied sedimentary basins are the Late Palaeozoic volcanic rocks (mainly Late Carboniferous–Early Permian), mainly consisting of basalt. They are widely distributed within the orogenic belts and sedimentary basins. These mantle-derived volcanic rocks are theoretically possible sources of the elevated $^3He/^4He$ ratios near the studied area. However, such extensive igneous rocks are all >250 Ma old (Zhang et al., 2010; Yu et al., 2012), and the local concentration of U and Th (Zhu et al., 2009) preclude the existence of high $^3He/^4He$ fluids being preserved in these rocks today.

There are post-collisional basalts localized along the periphery of the Tarim and Junggar Basin. Towards the south of the Tarim basin, Miocene-Holocene volcanic activity occurred in Kangxiwa (3.5 Ma, KXW), Dahongliutan (3.3 Ma, DHLT), Pulu (1.2 Ma, PL) and Ashikule (2–0 Ma, ASKL) within the Kunlun Mountains (Turner et al., 1996; Liu and Maimaiti, 1989; Chung et al., 2005). Towards the southwest Tarim basin, Eocene volcanism occurred in Piqiang (~40 Ma, PQ) and Tuoyun (~20 Ma, TY) within the southern part of the Tianshan Mountains (Luo et al., 2003). Towards the north Jungaar basin, Miocene volcanic activity occurred in Halaqiaola (~17 Ma, Huang et al., 2006). Kennedy and van Soest (2006) showed that Miocene (8–9 Ma) magmatic activity should not be considered as a source for mantle-derived helium in Dixie Valley, Nevada, with maximal R_c/R_a ratio of 0.7. Following the same considerations the small-scale Eocene-Miocene (40–20 Ma) volcanism in Xinjiang is not a viable source for the excess ^3He observed within the sedimentary basins. It is also unlikely that Pliocene volcanics in Kangxiwa, Dahongliutan and Pulu are a potential source for the elevated $^3He/^4He$ ratios because, given the very low ^4He concentrations expected in basalts (~10^{-9} cm^3 STP/g), after only ~1 Ma the addition of radiogenic ^4He will reduce the helium isotopic composition of a typical basalt to <0.1 R_a (Kennedy and van Soest, 2006).

However, the recent volcanic activities observed in Ashikule (most recent eruption was 27th May 1951: Liu and Maimaiti, 1989) cannot be ruled out for the potential source of excess ^3He. Given that this volcanic province is >400 km southeast of the Kekeya gas field where no clear ^3He excess is observed in samples Nos. 99–104 and 108–109 within the analytical errors, it is unlikely that the Ashikule volcanics would contribute to the elevated $^3He/^4He$ ratios in Akmomu gas field, 600 km from Ashikule. However, the possibility could be clarified by future gas study near Hetian (Fig. 2A).

5.1.3. Helium from mantle degassing

Based on the above discussion, it can be concluded that mantle helium degassing is required to explain the high $^3He/^4He$ datasets. The

most likely source for the mantle-derived helium in some of our samples is mantle-derived gases originating either from fluids or small scale melts in the upper asthenospheric or lithospheric mantle beneath the studied area.

The mantle-derived and crustal helium content in a gas samples can be therefore estimated based on the R_c/R_a ratio of gas sample. Taking the $^3He/^4He$ ratios of 8 R_a and 0.05 R_a for mantle and crustal helium end-member, respectively, the mantle-derived helium in Xinjiang gas samples varies from 0% to 7% (Table 1 and Figs. 3 and 5). It should be noted that the proportion of mantle-derived helium is also calculated for samples which have no available $^4He/^{20}Ne$, but instead high $^{40}Ar/^{36}Ar$ (e.g., >500). It is believed that such high $^{40}Ar/^{36}Ar$ is a proxy of negligible air contamination because all samples with relatively low $^{40}Ar/^{36}Ar$ (e.g., 300–500) but one sample No. 131 has $R/R_a < 0.05$ which is typical value for the crustal helium (Fig. 4). Although the $^{40}Ar/^{36}Ar$ ratio in sample No. 131 is as low as 329, its $^4He/^{20}Ne$ ratio (2113) is three orders of magnitude higher than the atmospheric value.

Thus, it is clear that the mantle signature shown in Table 1 and Fig. 5 is not very strong in Xinjiang when compared to those in sedimentary basins in eastern China. The much lower ratios in Xinjiang imply a lower mantle-derived ^3He flux.

5.2. Mantle He distribution in sedimentary basins and its tectonic implications

In the Tarim basin (Fig. 2A), the highest R/R_a of 0.6 is observed in the well Ake 1 in Akmomu gas field in the southwestern margin of the basin (sample Nos. 105–107). This is the highest $^3He/^4He$ ratio observed in the studied areas so far. Although the $^4He/^{20}Ne$ ratios are not available, a high $^{40}Ar/^{36}Ar$ ratio (1438 in sample No. 106) suggests negligible atmospheric contamination, indicating 7% mantle-derived helium. Low R_c/R_a and R/R_a (<0.05) are widely observed in the center of basins such as the Kuqa depressions, North depressions and Tazhong uplift, indicating nearly 100% of helium originates from the crust. In foreland sub-basins (Tabei uplift and southwest depression), the R_c/R_a and R/R_a values are between 0.02 and 0.6 (Fig. 2A), suggesting a purely crustal-radiogenic helium or a mixture of mantle-derived helium and crustal-radiogenic helium.

Fig. 2B shows the spatial distribution of $^3He/^4He$ ratios in the Junggar basin. Similarly, high R_c/R_a and R/R_a values (>0.1) are observed in foreland sub-basins (southern depression and west super uplift) located in front of the NE-E trending Tianshan (Bogda) Mountains and the N-NE trending Zhayier-Halalate Mountains. In contrast, low R_c/R_a and R/R_a values are widely distributed in the central depression of the basin.

Fig. 2C shows the $^3He/^4He$ ratio distribution in the Turpan-Hami basin. Although the spatial $^3He/^4He$ ratio distribution in the Turpan-Hami basin is not as clear as those in the Tarim and Junggar basins, the region's highest R/R_a is found in Well Hongtai2 (sample No. 168) in the Turpan depression which is located along the basin boundary faults in front of the Tianshan (Bogda) Mountains. Again, although there is no available $^4He/^{20}Ne$ ratio in this sample, the relatively high $^{40}Ar/^{36}Ar$ ratio (571) and helium concentration (693 ppm) likely suggest negligible atmospheric contamination, thus possibly reflecting ~1% input of mantle-derived helium.

Fig. 2D shows the $^3He/^4He$ ratio distribution in the Santanghu basin. Overall, the R_c/R_a values in the Santanghu basin are all <0.05, indicating purely crustal origin of helium.

In addition, Du et al. (1998) reported three R/R_a ranging between 0.02 and 0.34 in natural gases from the Yili basin (Fig. 1). Although the sampling location is not clear and no $^4He/^{20}Ne$ ratios were available, the highest R/R_a (0.34) might suggest the input of mantle-derived helium in this typical foreland basin.

In summary, there is a general $^3He/^4He$ distribution pattern in Xinjiang sedimentary basins, that is, mantle-derived helium are observed in the foreland sub-basins associated with the Tianshan, Kunlun and Zhayier-Halalate Mountains (Fig. 1), whereas pure crustal helium are distributed in the center of the basin. Such a spatial distribution of mantle-derived helium is similar to that observed in natural gas reservoirs in the foreland sub-basin of the west Texas Permian basin, where gases with high $^3He/^4He$ ratios (~0.5 R_a) and CO_2 contents (~55%) occur close to the thrust faults (Ballentine et al., 2001). A similar pattern was also found in the Polish and Ukrainian Flysch Carpathians and Mesozoic Basement of the Carpathian Foredeep basin (Kotarba and Nagao, 2008).

This suggests that mantle-derived helium is closely associated with the injection of mantle fluids or small scale melts beneath the orogenic zone. The foreland basin, located in the transitional structural zone between the orogenic belts and stable craton, is a type of basin formed by convergent compressional tectonic condition. One of the most obvious tectonic features in the foreland sub-basin is the occurrence of a series of imbricate thrust faults under which a number of oil/gas pools were formed. For example, high-resolution seismic reflection profile data show the complex thrust faults and Southwest Tianshan Basement Faults (~25 km deep) underneath the transition zone between the Tainshan Mountains and Tarim basin (Jiang et al., 2013). The main structure on the southern side of the Tianshan Mountains, is the Luntai fault zone, extending ~300 km southwest from Korle to Kashi (Fig. 2A). The ~3% mantle helium in samples Nos. 21–23 and ~7% in sample No. 106 are distributed along this fault zone (Fig. 5). The similar tectonic pattern can also be seen in the transitional structural zone between the Kunlun Mountains and Tarim basin near Hetian (Jiang et al., 2013), where the trace mantle helium (0.1%, sample Nos. 101–103 and 108–109) are observed. In the Junggar basin (Fig. 2B), the Ganhezhi-Santai faults extend several hundred kilometers west developed along the Tianshan Mountain. Along these faults in the southern depression, the mantle-derived helium is also up to ~3% (Nos. 131–133, Fig. 5). A large-scale NE-trending Karamay thrust fault with a length of ~250 km has developed between the western Junggar orogenic belt and the northwestern margin of the basin. The highest mantle-derived helium (~4%) along this fault is sample No. 144. In the Turpan-Hami basin, a nearly EW-running Central fault zone developed in front of the Tianshan Mountains, which consists of a series of reverse faults and extends over a distance of ~400 km. A sample with ~1% mantle-derives helium (No. 168) is located within these faults (Fig. 5). Such a $^3He/^4He$ distribution pattern suggests that leakage of mantle-derived helium through the sedimentary basin in Xinjiang is greater along the frontal faults than in areas far away from the faults. Thus, it can be concluded that these large, deep-seated fault zones are the key factor controlling the degassing of mantle-derived material, providing a direct conduit for the upwards migration of this material. The mantle-derived gases originating either from fluids or small scale melts in the upper asthenospheric or lithospheric mantle have found path ways into root zones of the major faults defining these basins, but do not significantly move into the basins themselves as evidenced by the purely crustal helium observed in there.

This close relationship between mantle-derived helium and major faults has been observed in other continental settings with compressional tectonics such as the San Andreas Fault in North America (Kennedy et al., 1997), the Median Tectonic Line in Japan (Doğan et al., 2006), the North Anatolian Fault in Turkey (Doğan et al., 2009), and the Karakoram Fault in Tibet (Klemperer et al., 2013). These observations have shown that mantle helium exsolves from partially-melted regions in the upper mantle, becomes focused into the root zones of major crustal faults, and subsequently traverses the crust via permeable fault zones. In the Itoigawa-Shizuoka Tectonic Line (ISTL) fault system (Umeda et al., 2013), $^3He/^4He$ ratios in gas samples distributed in the middle section have been found to be higher than those in the northern and southern sections. The middle ISTL is tectonically featured by strike-slip faulting, whereas the northern and southern ISTLs are characterized by reverse faulting. Such differences allowed authors to conclude that, compared with reverse faults under a compressional stress regime,

strike-slip faults serving as preferred permeable conduits could promote the effective transfer of mantle fluid to the Earth's surface.

It should be noted that there is a difference in the highest mantle-derived helium between the four basins: ~7% in Tarim, 4% in Junggar, possibly 1% in Turpan-Hami, and 0% in Santanghu basin. Although this variation may imply differences in the local mantle helium source, chemical compositions of the basement rocks, and local tectonics, local tectonic settings would be the most important factor in controlling distribution of mantle-derived helium within basin. For example, the scale of the thrust faults (i.e., fault inclination and distance from the magmatic reservoirs) might be considered as one of the most important factors controlling the transport of mantle-derived helium upwards to the gas reservoir.

5.3. CO_2 origins in the Tarim basin

As described above, CO_2 in hydrocarbon-rich natural gas in Xinjiang is essentially a trace component with concentration < 5% (Li et al., 2013). This is particularly true in the Junggar, Turpan-Hami and Santanghu basins. As a result, studies of the CO_2 sources have been paid less attention in comparison with the CO_2-rich gases in eastern China.

The trace CO_2 in hydrocarbon-rich gas reservoirs can be generally considered to have originated from the thermal decomposition of terrestrial and marine hydrocarbon-source organic matter. However, some samples with relatively high CO_2 concentration (>10%) found in the Akmomu gas field in the southwest depression and Luntai-Donghetang gas fields in the Tabei depression of the Tarim basin might have different sources in addition to organic origin.

In the Lunan-Donghetang gas field in the Tabei depression of the Tarim basin, the $^3He/^4He$ ratios of those CO_2-rich gases (24–25% in sample Nos. 25 and 33) have typical radiogenic values and thus suggest a typical crustal origin for the helium. Taking into account the local geological setting, the extensive occurrence of Cambrian-Ordovician marine carbonates most likely supports the thermal-decomposition of CO_2 from these carbonate rocks in the crust.

The CO_2 concentrations in the Akmomu gas reservoir reach 11–13% (sample Nos. 106 and 107). Based on one measured $\delta^{13}C$ value of CO_2 (−8.4‰), the CO_2 was produced by mixing of organic CO_2 and inorganic CO_2 derived from thermal decomposition of local marine carbonates (Zhang et al., 2005a). However, such a $\delta^{13}C$ value of CO_2 might alternatively show mixing of organic CO_2 and inorganic CO_2 originating from a mantle source whose $\delta^{13}C$ value is around −6.5‰ (Marty and Jambon, 1987). Occurrence of mantle-derived helium and argon in these CO_2-bearing gases supports this possibility.

As ^3He is an unambiguous tracer of magmatic volatiles and is carried by CO_2 as the mantle-derived melts upwards, the systematic behavior of $^3He/^4He$, $CO_2/^3He$ and $\delta^{13}C$ would allow us to identify the source of the CO_2. This is because the $CO_2/^3He$ ratio in continental environments should be similar to those observed in the convective mantle (~2×10^9, Marty and Jambon, 1987) if there is no significant contamination by crust-derived gases (>10^{10}, Marty and Jambon, 1987) or fractionation between carbon and helium. Such a case was observed in natural gases from the foreland sub-basin in the west Texas Permian basin (Ballentine et al., 2001). Therefore, further systematic study of carbon and helium chemical and isotopic compositions on these CO_2-bearing gases in Tarim basin would be a key to clarify the origin of CO_2.

6. Conclusions

The noble gas isotope compositions in gas samples indicate that as much as approximately 7% of the helium in the crust of Xinjiang is mantle-derived. The mantle-derived helium is generally observed in foreland sub-basins which are considered to be associated with the injection of mantle-derived gases originating either from fluids or small scale melts in the upper asthenospheric or lithospheric mantle beneath the orogenic mountains through major thrust faults. Typical crustal helium is extensively distributed in the center of each sedimentary basin. This study confirms previous findings that the major faults play an important role in transporting mantle-derived components to the surface in non-volcanic and tectonically compressional regions.

Acknowledgments

This study was partly supported by the National Natural Science Foundation of China (41273112), Chinese Academy of Sciences (KZCX2-XB3-12) and China National Key Basic Research and Development Program "973" (2011CB201102). We are grateful for the constructive comments from Dr. S. L. Klemperer and one anonymous reviewer. Our thanks are also extended to Drs S. L. Klemperer and B. Tripney for English corrections.

References

Ballentine, C.J., Schoell, M., Coleman, D., Cain, B.A., 2001. 300-Myr-old magmatic CO_2 in natural gas reservoirs of the west Texas Permian basin. Nature 409, 327–331.
Burnard, P., Bourlange, S., Henry, P., Geli, L., Tryon, M.D., Natal'in, B., Sengör, A.M.C., Özeren, M.S., Çagatay, M.N., 2012. Constraints on fluid origins and migration velocities along the Marmara Main Fault (Sea of Marmara, Turkey) using helium isotopes. Earth Planet. Sci. Lett. 341–344, 68–78.
Cao, J., Wang, X.L., Sun, P.A., Zhang, Y.Q., Tang, Y., Xiang, B.L., Lan, W.F., Wu, M., 2012. Geochemistry and origins of natural gases in the central Junggar Basin, Northwest China. Org. Geochem. 53, 166–176.
Chung, S.L., Chu, M.F., Zhang, Y.Q., Xie, Y.W., Lo, C.H., Lee, T.Y., Lan, C.Y., Li, X.H., Zhang, Q., Wang, Y.Z., 2005. Tibetan tectonic evolution inferred from spatial and temporal variations in post-collisional magmatism. Earth-Sci. Rev. 68, 173–196.
Dai, J.X., Wu, X.Q., Ni, Y.Y., Wang, Z.C., Zhao, C.Y., Wang, Z.Y., Liu, G.X., 2012. Geochemical characteristics of natural gas from mud volcanoes in the southern Junggar Basin. Sci. China Earth Sci. 55, 355–367.
Doğan, T., Sumino, H., Nagao, K., Notsu, K., 2006. Release of mantle helium from the forearc region of the Philippine Sea plate subduction. Chem. Geol. 233, 235–248.
Doğan, T., Sumino, H., Nagao, K., Notsu, K., Tuncer, M.K., Çelik, C., 2009. Adjacent releases of mantle helium and soil CO_2 from active faults: observations from the Marmara region of the north Anatolian fault zone, Turkey. Geochem. Geophys. Geosyst. 10, Q11009.
Du, J.G., Xu, Y.C., Sun, M.L., 1998. Helium isotopes and heat flow in the oil and gas bearing basins in China's continent. Acta Geophys. Sin. 41, 495–501 (in Chinese with English abstract).
Duan, Y., Zheng, Z.Y., Duan, X.C., Wang, Z.Y., Zhang, S.B., 2007. Helium isotopic evidence of natural gas formation and migration in Tazhong gas field. Nat. Gas Ind. 27, 28–30 (in Chinese).
Fu, B., Lin, A.M., Kano, K., Maruyama, T., Guo, J.M., 2003. Quaternary folding of the eastern Tian Shan, northwest China. Tectonophysics 369, 79–101.
Gao, S., Luo, T.C., Zhang, B.Z., Zhang, H.F., Han, Y.W., Zhao, Z.D., Hu, Y.K., 1998. Chemical composition of the continental crust as revealed by studies in East China. Geochim. Cosmochim. Acta 62, 1959–1975.
Gao, R., Hou, H., Cai, X., Knapp, J.H., He, R., Liu, J., Xiong, X., Guan, Y., Li, W., Zeng, L., Roecker, S.W., 2013. Fine crustal structure beneath the junction of the southwest Tian Shan and Tarim Basin, NW China. Lithosphere 5, 382–392.
Guo, B., Liu, Q.Y., Chen, J.H., Zhao, D.P., Li, S.C., Lai, Y.G., 2006. Seismic tomography of the crust and upper mantle structure underneath the Chinese Tianshan. Chin. J. Geophys. 49, 1693–1700 (in Chinese with English abstract).
Huang, B., Piper, J.D.A., He, H., Zhang, C., Zhu, R., 2006. Paleomagnetic and geochronological study of the Halaqiaola basalts, southern margin of the Altai Mountains, northern Xinjiang: constraints on neotectonic convergent patterns north of Tibet. J. Geophys. Res. 111, B01101. http://dx.doi.org/10.1029/2005JB003890.
Jiang, X., Li, Z., Li, H., 2013. Uplift of the west Kunlun range, northern Tibetan plateau, dominated by brittle thickening of the upper crust. Geology 41, 439–442.
Kennedy, B.M., van Soest, M.C., 2006. A helium isotope perspective on the Dixie Valley, Nevada, hydrothermal system. Geotherm. 35, 26–43.
Kennedy, B.M., Kharaka, Y.K., Evans, W.C., Ellwood, A., DePaolo, D.J., Thordsen, J., Ambats, G., Mariner, R.H., 1997. Mantle fluids in the San Andreas fault system, California. Science 278, 1278–1281.
Klemperer, S.L., Kennedy, B.M., Sastry, S.R., Makovsky, Y., Harinarayana, T., Leech, M.L., 2013. Mantle fluids in the Karakoram fault: helium isotope evidence. Earth Planet. Sci. Lett. 366, 59–70.
Kotarba, M.J., Nagao, K., 2008. Composition and origin of natural gases accumulated in the Polish and Ukrainian parts of the Carpathian region: gaseous hydrocarbons, noble gases, carbon dioxide and nitrogen. Chem. Geol. 255, 426–438.
Li, T., 1995. Element abundances of China's continental crust and its sedimentary layer and upper continental crust. Chin. J. Geochem. 14, 26–32.
Li, J., Li, Z.S., Wang, D.L., Li, J., Cheng, H.G., Xie, Z.Y., Wang, X.B., Sun, Q.W., 2013. Geochemical characteristics and N_2 source of natural gas in Tarim basin. Acta Pet. Sin. 24, 102–111 (in Chinese with English abstract).
Liu, J.J., Maimaiti, Y., 1989. Distribution and ages of Ashikule volcanoes on the West Kunlun Mountains, west China. Bull. Glacier Res. 7, 187–190.
Liu, Q.Y., Dai, J.X., Jin, Z.J., Li, J., 2009. Geochemistry and genesis of natural gas in the foreland and platform of the Tarim basin. Acta Geol. Sin. 83, 107–114.

Luo, Z.H., Bai, Z.D., Zhao, Z.D., Zhan, H.M., Li, L., 2003. Cenozoic magmatism in the south and north rimas of Tarim basin: petrogenesis and tectonic implications. Earth Sci. Front. 10, 179–189 (in Chinese with English abstract).
Mamyrin, B.A., Tolstikhin, I.N., 1984. Helium Isotope in Nature. Elsevier (273p).
Marty, B., Jambon, A., 1987. $C/^3He$ in volatile fluxes from the solid Earth: implications for carbon geodynamics. Earth Planet. Sci. Lett. 83, 16–26.
O'Nions, R.K., Oxburgh, E.R., 1988. Helium, volatile fluxes and the development of continental crust. Earth Planet. Sci. Lett. 90, 331–347.
Qin, S.F., 1999. The genesis of abnormal natural gas in Kuqa depression. Explorationist 4, 21–23 (in Chinese).
Qiu, N.S., Zhang, Z.H., Xu, E.S., 2008. Geothermal regime and Jurassic source rock maturity of the Junggar Basin, northwest China. J. Asian Earth Sci. 31, 464–478.
Sano, Y., Nakamura, Y., Wakita, H., Urabe, A., Tominaga, T., 1984. ^3He emission related to volcanic activity. Science 224, 150–151.
Sano, Y., Wakita, H., Ohsumi, T., Kusakabe, M., 1987. Helium isotope evidence for magmatic gases in Lake Nyos, Cameroon. Geophys. Res. Lett. 14, 1039–1041.
Shen, P., Zhu, H.Y., Xu, Y.C., 1983. Distributional features of uranium, thorium and potassium in the sedimentary rocks. Acta Sedimentol. Sin. 1, 109–122 (in Chinese with English abstract).
Tao, M.X., 2010. The two kinds of tectonic unit systems in Turpan-Hami basin, Xinjiang, China. Geol. Bull. China 29, 297–304 (in Chinese with English abstract).
Tao, M.X., Xu, Y.C., Shi, B.G., Jiang, Z.X., Shen, P., Li, X.B., Sun, M.L., 2005. Mantle degassing in different types of faults and deep geological and tectonic characteristics. Sci. China Earth Sci. 35, 441–451 (in Chinese).
Tao, H.F., Wang, Q.C., Yang, X.F., Lin, J., 2013. Provenance and tectonic setting of late Carboniferous clastic rocks in west Junggar, Xinjiang, China: a case from the Hala-alat Mountains. J. Asian Earth Sci. 64, 210–222.
Turner, S., Arnaud, N., Liu, J., Rogers, N., Hawkesworth, C., Harris, N., Kelley, S., Van Calsteren, P., Deng, W., 1996. Post-collision, shoshonitic volcanism on the Tibetan plateau: implications for convective thinning of the lithosphere and the source of Ocean Island basalts. J. Petrol. 37, 45–71.
Umeda, K., Ninomiya, A., 2009. Helium isotopes as a tool for detecting concealed active faults. Geochem. Geophys. Geosyst. 10, Q08010.
Umeda, K., Ninomiya, A., McCrank, G.F., 2008. High ^3He emanations from the source regions of recent large earthquakes, Central Japan. Geochem. Geophys. Geosyst. 9, Q12003.
Umeda, K., Asamori, K., Kusano, T., 2013. Release of mantle and crustal helium from a fault following an inland earthquake. Appl. Geochem. 37, 134–141.
Wang, Z.M., Wang, Q.H., Zhao, M.J., Li, Y., Xu, Z.M., 2008. Characteristics, genesis and accumulation history of natural gas in Hetianhe gasfield, Tarim Basin, China. Sci. China Earth Sci. 51, 84–95.
Xu, Y.C., 1994. Theory and Application of Natural Gas Formation. Science Press, p. 424 (in Chinese).
Xu, S., Nakai, S., Wakita, H., Xu, Y.C., Wang, X.B., 1995. Helium isotope compositions in sedimentary basins in China. Appl. Geochem. 10, 643–656.
Xu, Y.C., Shen, P., Liu, W.H., Tao, M.L., Su, M.L., Du, J.G., 1998. Noble Gas Geochemistry in Natural Gases. Science Press, p. 231 (in Chinese).
Xu, Y., Liu, F.T., Liu, J.H., Sun, R.M., 2001. Seismic tomography beneath the orogenic belts and adjacent basins of northwestern China. Sci. China Earth Sci. 44, 468–480.
Yu, S., Zhang, S.C., Shi, J.A., Zhi, D.M., Sun, G.Q., 2012. Tectonic settings of the late Carboniferous – early Permian volcanics, central Junggar Basin. Chin. J. Geol. 47, 1005–1015 (in Chinese with English abstract).
Zhang, J.F., Wang, D.L., Wang, Z.M., Li, X., Su, X.F., 2005a. Natural gas deposit formation geochemistry of Akmomu gas field, Kashi Sag in Tarim basin. Nat. Gas Geosci. 16, 507–513 (in Chinese with English abstract).
Zhang, D.W., Liu, W.H., Zheng, J.J., Wang, X.F., Nan, Q.Y., 2005b. Helium and argon isotopic compositions of natural gases in the Tazhong area, Tarim Basin. Pet. Explor. Dev. 32, 38–41 (in Chinese with English abstract).
Zhang, M.M., Chen, H.H., Zheng, J.P., Su, Y.P., 2010. The age of Kalagang formation in the Santanghu basin, Northeast Xinjiang: evidence from Ziron U-Pb dating of volcanic rocks. Bull. Mineral. Petrol. Geochem. 29, 400–408 (in Chinese with English abstract).
Zhao, J.M., Liu, G.D., Lu, Z.X., Zhang, X.K., Zhao, G.Z., 2003. Lithospheric structure and dynamic processes of the Tianshan orogenic belt and the Junggar basin. Tectonophysics 376, 199–239.
Zheng, J.J., Sun, G.Q., Sun, S.L., Liu, W.H., 2004. Comparison of helium isotopes in Tarim basin and eastern China basins. Nat. Gas Ind. 24, 26–29 (in Chinese).
Zheng, J.J., Liu, W.H., Sun, G.Q., Cao, C.P., Hu, H.F., Xu, Y.C., 2005. Helium isotopes and tectonic implications in stable and sub-stable tectonic basins. Prog. Nat. Sci. 15, 951–957 (in Chinese).
Zhu, Y.F., Guo, X., Song, B., Zhang, L.F., Gu, L.B., 2009. Petrology, Sr–Nd–Hf isotopic geochemistry and zircon chronology of the late Palaeozoic volcanic rocks in the southwestern Tianshan Mountains, Xinjiang, NW China. J. Geol. Soc. 166, 1085–1099.